This is a post-peer-review, pre-copyedit version of an article published in MAGMA.
The final authenticated version is available online at: http://dx.doi.org/10.1007/s10334-017-0670-8

Single-Breath-Hold Abdominal T_1 Mapping using 3-D Cartesian Look-Locker with Spatio-Temporal Sparsity Constraints

Felix Lugauer[1], Jens Wetzl[1], Christoph Forman[2], Manuel Schneider[1], Berthold Kiefer[2], Joachim Hornegger[1], Dominik Nickel[2] and Andreas Maier[1]

Affiliations:

1 Pattern Recognition Lab, Department of Computer Science, Friedrich-Alexander-Universität Erlangen-Nürnberg, Erlangen, Germany

2 Siemens Healthcare GmbH, Diagnostic Imaging, Erlangen, Germany

Notes:

Running Head: Single-Breath-Hold T_1 Mapping via 3-D LL

Correspondence to: Felix Lugauer
Pattern Recognition Lab,
(Department of Computer Science),
Friedrich-Alexander-Universität Erlangen-Nürnberg,
Martensstr. 3, D-91058 Erlangen, Germany.
E-mail: felix.lugauer@fau.de
Phone: +49 9131 85 27874
Fax: +49 9131 303811

Word count:

Abstract:	200	Manuscript:	ca. 5600
Figures:	9	Tables:	3
References:	39		

ABSTRACT

Object: To develop and validate a 3-D Cartesian Look-Locker T_1 mapping technique that achieves high accuracy and whole-liver coverage within a single breath-hold.

Materials and Methods: The proposed method combines sparse Cartesian sampling based on a novel spatio-temporally incoherent Poisson pattern and k-space segmentation, dedicated for high temporal resolution imaging. This combination allows capturing tissue with short relaxation times with volumetric coverage. A joint reconstruction of the 3-D+TI data via compressed sensing exploits the spatio-temporal sparsity and ensures consistent quality for the subsequent multi-step T_1 mapping. Data from the NIST phantom and 11 volunteers along with reference 2-D Look-Locker acquisitions are used for validation. 2-D and 3-D methods are compared based on T_1 values in different abdominal tissues for 1.5 and 3 T systems.

Results: T_1 maps obtained from the proposed 3-D method compare favorably with those from the 2-D reference and additionally allow for reformatting or volumetric analysis. Excellent agreement is shown in phantom ($bias_{3T}$ < 2%, $bias_{1.5T}$ < 5% for [120;2000] ms) and volunteer data (3-D and 2-D deviation < 4% for liver, muscle and spleen) for clinically acceptable scan (20 s) and reconstruction times (< 4 min).

Conclusion: Whole-liver T_1 mapping with high accuracy and precision is feasible in one breath-hold using spatio-temporally incoherent sparse 3-D Cartesian sampling.

Key words: T_1 mapping, 3-D Look-Locker, Compressed sensing, Poisson sampling

INTRODUCTION

Quantitative maps of the longitudinal relaxation (T_1) can provide diagnostic information for a large set of pathologies throughout the whole body. With respect to abdominal diseases, T_1 mapping is used for detecting chronic pancreatitis, assessing liver function as well as function of native and transplanted kidneys [1–4]. Despite the fact that the T_1 relaxation can serve as a quantitative biomarker, its widespread use in clinical practice is hampered by particularly long acquisition times that are required for accurate T_1 quantification. For the prevailing gold standard method, inversion recovery (IR), the relaxation curve is repeatedly sampled at a single time point after an inversion or saturation pulse, followed by a waiting period for full relaxation. This time period can be tremendous as it is determined by the tissue with the longest T_1 ($\sim 5T_1$). Considerably faster acquisitions are possible with the method by Look and Locker (LL) [5], which samples the relaxation curve at multiple time points after inversion and corrects for the effects of the continuous readout [6]. Alternatively, it is common to quantify T_1 by using variable flip angle (VFA) images in combination with an additional B_1 correction scan [7]. While this approach makes volumetric mapping feasible even in single breath-holds [3, 8], its accuracy degrades with higher field-strengths and higher T_1 values [9].

In today's clinical practice, abdominal T_1 mapping is performed either for few slices without volumetric coverage based on IR or LL [2, 4], or with volumetric coverage using the VFA method, ideally within a single breath-hold [1, 3]. However, single or multiple 2-D measurements with partial coverage are suboptimal for various reasons: First, smaller organs can easily be missed, particularly in case of patient movement or obliquely extending organs. Second, the signal-to-noise ratio (SNR) is inherently lower than in 3-D acquisitions, which affects the precision of T_1 quantification, thereby reducing its discriminating value as a biomarker. Third, T_1 could be inhomogeneous throughout the organ, which is known to occur in the liver [3]. Thus, volumetric T_1 mapping based on an accurate IR or LL method that can be performed in 20 s would be highly desirable.

Even though 3-D extensions of LL exist, they require acquisition times in the order of several minutes due to segmented sampling with delays for undisturbed (partial) relaxation, limiting its application to static imaging, e.g., of the head or knee [10, 11]. It is worth noting that although partial relaxation increases the scan efficiency compared to full relaxation, it limits the dynamic range and further increases the B_1 sensitivity. Alternatively, multi-slice LL strategies can utilize the free relaxation delay in other slices to capture a series of 2-D measurements very efficiently [12, 13]. The advent of compressed sensing opened up the possibility of shortening scan time beyond what was possible with parallel imaging alone [14]. Initially largely applied to qualitative imaging, it was found that even sparser sampling is possible when sparsity in other dimensions such as time or contrast is additionally used [15, 16]. Here, the approach of Doneva et al. stands out as one of the first dictionary-based reconstructions [17]. In theory, many of these approaches are technically related

since they try to enforce certain constraints, e.g. differences along the parametric dimension, either more (dictionary) or less (finite differences) explicitly. In the context of T_1 mapping, sparse methods were mainly employed to accelerate 3-D VFA mapping or only 2-D LL approaches [16–19]. Recently, a non-Cartesian spiral acquisition with through-time GRAPPA by Chen et al. demonstrated volumetric LL-based T_1 mapping for the first time in a breath-hold [20].

In this work, we aim to achieve the volumetric coverage of VFA methods with the accuracy of LL-based methods in order to perform breath-held volumetric T_1 mapping. To this end, we combine an accurate 3-D LL scheme based on k-space segmentation with sparse incoherent sampling in space and time. A compressed sensing reconstruction with spatio-temporal wavelet regularization that has been successfully employed for 3-D CINE imaging ensures sufficient quality for subsequent T_1 fitting despite high acceleration factors [21]. A main advantage of our method over recent work is that a self-contained volumetric T_1 mapping is feasible in a single breath-hold where no further time-consuming calibration scan is required. Validation of the proposed method is demonstrated based on 2-D reference data using both phantom and in-vivo experiments. A preliminary version of this work has been presented previously [22].

MATERIALS AND METHODS

Our proposed acquisition follows a Look-Locker scheme, which samples the relaxation continuously with low flip-angle (FA) pulses after increasing the dynamic range by an adiabatic inversion pulse [6]. To sample a larger number of phase-encoding steps along a desired time interval of the relaxation curve, k-space is divided into S segments. In turn, following the original model (details in subsection *Multi-step T_1 mapping*), this requires $S - 1$ time delays (TD) for full relaxation in order to provide equal magnetization before each repeated inversion pulse [20]. Figure 1 outlines the concept of this segmented acquisition.

Sparse Cartesian sampling with spatio-temporal incoherence

In order to achieve the temporal resolution to properly observe the relaxation curve even for tissues with very fast relaxation, the images are sparsely sampled with spatio-temporal incoherence during the inversion time (TI) interval. To this end, we extended a fast 2-D Poisson sampling [23] to feature variable density (VD) as well as variable incoherence along a sequence of generated patterns. Compared to VD Poisson sampling [24, 25], the main advantage of the joint computation of all k-space sampling patterns at different TIs is a better coverage for the collapsed (accumulated) k-space of the complete measurement and less overlap between consecutive TIs. For view sharing, a technically related approach for a complementary Poisson sampling was recently proposed [25].

Generating a two-dimensional sampling pattern for the phase-encoding steps is based on [23]

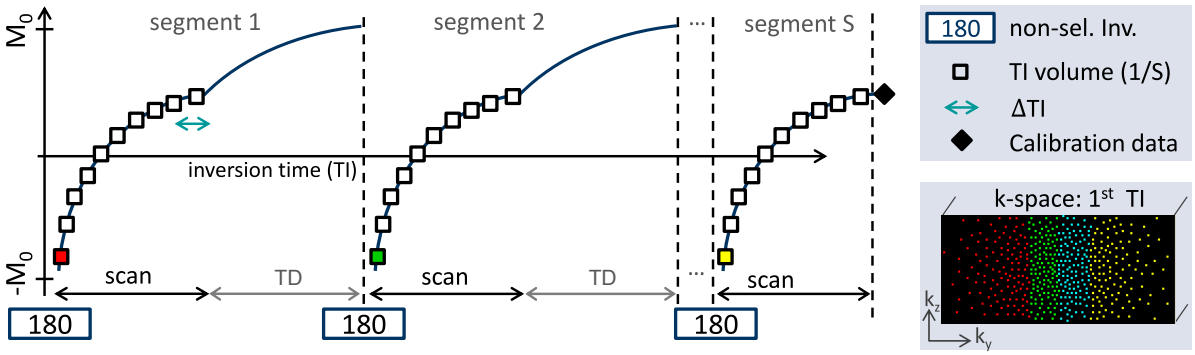

FIG. 1 The measurement of the relaxation is repeated by the number of segments that are used to partition the k-space in order to accommodate a 3-D phase encoding with high temporal resolution. Except for the last, each partial acquisition that drives magnetization into a steady state is followed by a constant delay time (TD), in which the relaxation to the initial magnetization can occur. At the end of the acquisition, calibration data for the coil sensitivity map of the SENSE reconstruction is acquired

to greatly accelerate the sampling process. Our variable density pattern is incorporated by scaling the radius r, which is associated with the centered position $\boldsymbol{p} = (p_y, p_z)$ with $p_y \in [-0.5N_y, 0.5N_y)$ and $p_z \in [-0.5N_z, 0.5N_z)$ by the reciprocal of a density-like function,

$$\hat{\rho}(\boldsymbol{p}) = \left(1 - \frac{\overbrace{\sqrt{p_y^2 + (p_z a)^2}}^{\text{distance to center}}}{\underbrace{s\sqrt{(0.5N_y)^2 + (0.5N_z a)^2}}_{\text{normalization}}}\right)^{\nu}, \tag{1}$$

using the distance to the k-space center on a grid with aspect ratio $a = N_y/N_z$. The scale factor $s \geq 1$ (fixed to $s = 1.2$) in front of the normalization factor is used to adjust for the zero drop-off at corner regions. The degree of variable density is controlled by the exponent ν (typically $\nu = 2$). Thus, the density at the border compared to the center is

$$\frac{\hat{\rho}|_{border}}{\hat{\rho}|_{center}} = \left(1 - \frac{\sqrt{(N_y - 1)^2 + a^2(N_z - 1)^2}}{s\sqrt{N_y^2 + N_z^2 a^2}}\right)^{\nu}. \tag{2}$$

Finally, the density $\hat{\rho}$ is scaled such that the accumulation of all values on the grid matches the desired number of sampling points, i.e. $N_p = N_y N_z / AF$ for the specified acceleration factor (AF):

$$\rho(\boldsymbol{p}) = \hat{\rho}(\boldsymbol{p}) \frac{N_p}{\sum_{\boldsymbol{q}} \hat{\rho}(\boldsymbol{q})}. \tag{3}$$

Elliptical or fully sampled masks can be induced by setting the density at the respective position close to zero or one.

By keeping track of sampled positions for all N TI images in an accumulated mask $\boldsymbol{M}_a \in \mathbb{N}^{N_y \times N_z}$, initialized by zero, and by adhering to a further discard rule during disc generation, the

number of duplicate positions can be minimized while still maintaining Poisson properties:

$$\boldsymbol{M}_a(\boldsymbol{p}) \leq \underbrace{\rho(\boldsymbol{p}) \cdot n}_{\text{density constraint}} + \overbrace{(1-\theta)+\epsilon}^{\text{relaxes constraint}}, \tag{4}$$

where $\theta \in [0,1]$ controls the degree of incoherence for the current image $n \in [1,N]$. The density constraint $\rho(\boldsymbol{p}) \cdot n$ denotes the targeted density when generating the n-th image. The rational behind this rule is that when θ is close to 1, only points that would contribute to a currently undersampled density w.r.t. the targeted density are accepted. For such high values, the addition of a small $\epsilon \approx 0.01$ is useful to relax this constraint in order to avoid concentric clusters or gaps in the pattern [25]. That means, for smaller θ the temporal incoherence gradually relaxes while spatial Poisson properties are maintained. The complete Poisson generator is summarized under Algorithm 1 in the Appendix and code is openly available online: `https://github.com/sifeluga/PDvdi`. Note that the final number of points can slightly vary due to the randomized processes but a deterministic number of samples is required to warrant a subsequent k-space segmentation. Viable options are to correct the number of points afterwards or to scale ρ to produce slightly more samples but stop the generation when the number of desired points is reached. The effect of the temporal incoherence is shown in Figure 2 for generating a k-space sequence of 10 TIs with the accumulated mask on the left and the distinct k-spaces for increasing TIs on the right. Using temporal incoherence (bottom), the number of duplicates (red)—points sampled more than once—was reduced and the k-space coverage (yellow)—points sampled once—was increased.

Segmentation and reordering

The segmentation and reordering strategy affects the image contrast in several ways. One possible effect is that neighboring points in k-space can end up with very different effective sampling times leading to artifacts in the final image [26]. Another source of error are large gradient amplitudes induced by oscillating positions in the phase-encoding plane, which can be reduced by keeping gradient moments between consecutively sampled points small [27]. Since a high dynamic range of the observed relaxation can improve the fit accuracy, a contrast that is formed as early as possible is particularly advantageous for short T_1 values. Possible schemes of segmentation and reordering are illustrated in Figure 3. While a "linear" encoding with a higher time to k-space center is more sensitive to artifacts [27], other schemes such as an "onion"-like segmentation [26] can suffer from greatly varying gradient amplitudes between segments.

We thus favor a strategy that achieves both distance minimization between subsequently sampled points and consistent reordering with an early acquired k-space center [27]. This can be achieved by a "wedge" segmentation, which has recently been used to optimize the scan efficiency for MP-Rage imaging [28]. To this end, points in the phase-encoding plane are ordered by their angle

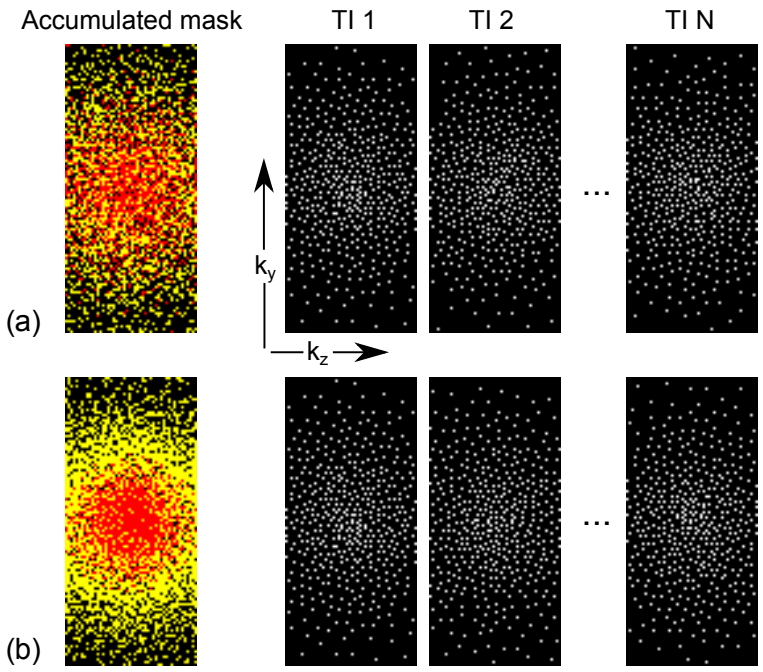

FIG. 2 Generating a sequence of Poisson patterns independently can yield high correlations between patterns, resulting in a substantial amount of duplicates and at the same time leave many positions uncovered over the course of contrasts (a). With the inclusion of an additional rule during point generation, the temporal incoherence can variably (θ) be increased. For an exemplary setup (N_y=110, N_z=50, N=10, AF=12, $\nu = 2$) and $\theta = 0.75$, the number of duplicates (red)—points sampled more than once—reduced from 33% to 21% while the coverage (yellow)—points sampled once—increased from 52% to 63% (b)

to the k-space center and partitioned into S equally numbered "wedges". The reordering of each wedge starts at the center and extends outwards by traversing points alternatingly in between the wedge's angular bounds (see Figure 3 (c,f)). Compared to other schemes, the average distance between sampled points is minimized. Since the TI time associated to a reordering is not strictly defined, we determined the time to center for each sampling scheme experimentally through inspection of relaxation curves with known T_1 values.

Data reconstruction

The 3-D data of all TI images was reconstructed jointly in order to exploit the temporal similarity between adjacent contrasts during a time-resolved (3-D+t) reconstruction [21]. A SENSE based nonlinear iterative reconstruction with spatio-temporal regularization via Haar wavelets was used [29]. For convenience, the four-dimensional data was decoupled along the fully sampled readout direction and reconstructed as N_x vectors of 2-D+t concatenated TI images $\boldsymbol{x}_i = \left[\boldsymbol{x}(1)_i^T, \ldots, \boldsymbol{x}(N)_i^T\right]^T \in$

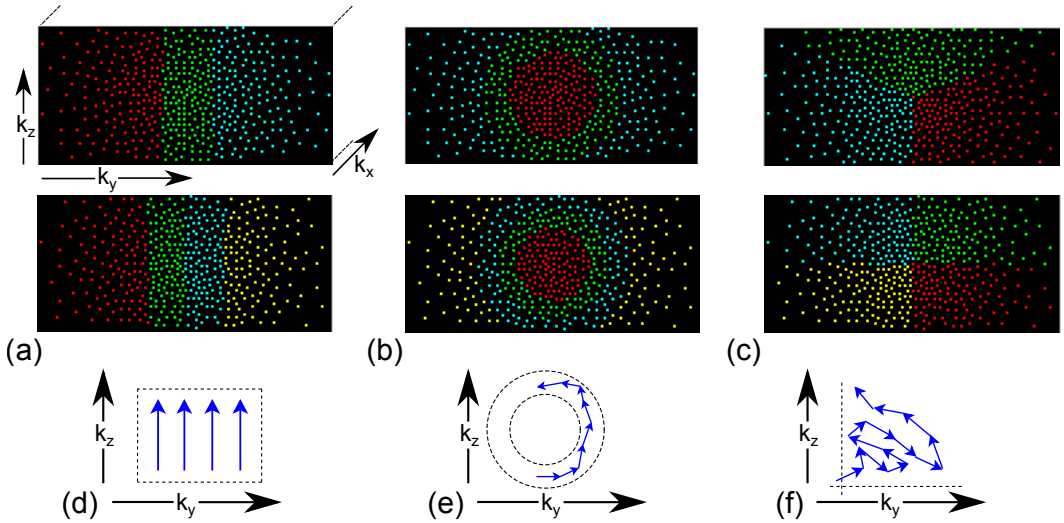

FIG. 3 Exemplary k-space segmentations along with possible reordering schemes for traversal: "linear" (a), "onion" (b) and "wedge" (c) segmentations with 3 and 4 segments. Each strategy is accompanied by particular reordering strategies (d)-(f). The combination of both defines the actual sampling order, which affects gradient magnitudes and image contrast. For a typical k-space with 4 segments and variable density (N_y = 110, N_z = 50, AF = 12, ν = 2), the average distance for traversing all points is 11.6, 4.9 and 4.5 for the "linear", "onion" and "wedge" sampling scheme

$\mathbb{C}^{N_y N_z \cdot N}$, $i \in [1, N_x]$ with the following cost function,

$$\boldsymbol{x}_i = \underset{\hat{\boldsymbol{x}}_i}{\operatorname{argmin}} \sum_{n=1}^{N} \sum_{c=1}^{C} \frac{1}{2} \left\| \boldsymbol{U}_n \boldsymbol{\mathcal{F}} \boldsymbol{S}_c \hat{\boldsymbol{x}}(n)_i - \boldsymbol{y}(n)_c \right\|_2^2 + \left\| \boldsymbol{W}_{(\sigma,\tau)} \hat{\boldsymbol{x}}_i \right\|_1 , \tag{5}$$

where $\boldsymbol{S}_c$ denotes the coil sensitivity matrix, $\boldsymbol{\mathcal{F}}$ the Fourier transform and $\boldsymbol{U}_t$ the undersampling matrix which are applied to current image estimate $\hat{\boldsymbol{x}}(n)_i$ to calculate the difference to the measured data $\boldsymbol{y}(n)_c$ for coil and time index c and n, respectively. $\boldsymbol{W}_{(\sigma,\tau)}$ denotes a single-level Haar wavelet transformation in the phase- and time-encoding directions. A FISTA scheme was used to optimize the cost function [30, 31], which was implemented using proximal algorithms. Consequently, the solution of the proximal operator for the wavelet regularization is a shrinkage of wavelet coefficients [32]. Similarly to level-dependent shrinkage, this offers the possibility of different thresholds, λ_σ and λ_τ, for low- and high-frequency coefficients in the final, i.e. temporal, transform dimension [31]. In what follows, they are denoted spatial and temporal regularization weights.

Multi-step T_1 mapping

Spoiled gradient echoes (GRE) are used to acquire readouts with low flip angles, i.e. FLASH imaging, and, thus, the signal model for 2-D LL by Deichmann et al. is applicable [6]. This holds only if sufficient delay for full relaxation is scheduled in between segments [20]. Effects of insufficient delay are discussed below.

A short revisit of [6] helps to appreciate that despite a high flip angle dependence, knowledge of the actual excitation can be circumvented. The signal at time TI after a (perfect) 180° inversion pulse is dependent on the initial and steady-state magnetization M_0 and M_{SS} as well as the effective relaxation ${T_1}^*$:

$$M(TI) = M_{\mathrm{SS}} - (M_0 + M_{\mathrm{SS}})\mathrm{e}^{-TI/T_1^*}. \tag{6}$$

The relation between effective and true relaxation is a function of TR and flip angle (FA) α,

$$\frac{1}{T_1^*} = \frac{1}{T_1} - \frac{1}{TR \cdot \log(\cos\alpha)}. \tag{7}$$

For calculating T_1 using the above equation, knowledge of the actual FA is required, which can largely deviate from the nominal value, e.g., due to B_1 field inhomogeneities. However, observing the relaxation at sufficient time points N and using the model reformulation $M(TI) = a - b\mathrm{e}^{-TI/T_1^*}$ can yield T_1 without knowledge of the actual FA by

$$T_1 = T_1^*(b/a - 1)\,, \tag{8}$$

after a voxel-wise non-linear least squares fit for $a, b \in \mathbb{C}$ and $T_1^* \in \mathbb{R}$:

$$\min_{a,b,T_1^*} \sum_{n=1}^{N} \left(\boldsymbol{x}(n) - \left| a - b\mathrm{e}^{-TI_n/T_1^*} \right| \right)^2. \tag{9}$$

Naturally, this requires that a point in time TI_n is associated to every image $\boldsymbol{x}(n)$, i.e. when the image contrast is formed. Yet, the formation of contrast is dependent on the actual segmentation and reordering strategy, which then also influences the T_1 value. Thus, a consistent way of selecting TI is required. We opted to calibrate the initial TI (latter ones depend on TI_1 and TR) based on actual measurements of the T_1 phantom: TI_1 was chosen to minimize the overall error to known T_1 values in the range of 120 to 2000 ms (cf. Sec. Experiments).

It is important to note that in case of a segmented acquisition, T_1 can only accurately be determined when the wait time (TD) is long enough for full relaxation before acquiring the next segment. While this does not affect the exponential parameter T_1^*, a reduced starting magnetization M_0 changes the correction term b/a such that the induced T_1 error is directly proportional to the percentual relaxation. This can be simulated for various T_1 from Eqs. (6) and (7) dependent on TR, α, the acquisition window and TD [20].

As later described by Deichmann [33], the actual FA can be extracted from Eq. (7), which can be used to fit the data more robustly to a model with only two parameters T_1^* and M_0,

$$M(TI) = M_0 \left(1 + \frac{T_1^*}{TR}\log(\cos\alpha) - \left(2 + \frac{T_1^*}{TR}\log(\cos\alpha)\right)\mathrm{e}^{-TI/T_1^*} \right). \tag{10}$$

This lends itself to a multi-step algorithm, where the common assumption of a smoothly varying B_1 field can be imposed on the flip angle distribution [26]. After the initial three-parameter fit, the

Protocol	2-D	3-D 1.5 T	3-D 3 T	3-D 1.5 T (high-res)
Figure #	5	5 to 9	4, 5, 8 and 9	8
TE/TR [ms]	1.3/2.9	0.7/1.9	0.8/2.0	0.9/2.1
Flip angle [°]	8	3	2.5	3
Bandwidth [Hz]	1530	1490	1530	1490
FOV [cm]	37×27	$37\pm1 \times 27\pm3 \times 18$	$37\pm3 \times 27\pm3 \times 18$	$35 \times 26 \times 16$
Resolution [mm]	1.9×2.3*	2.2×2.2	2.3×2.3	1.8×2.0
Thickness [mm]	8	6	6	5
Sampling [%]	100	100/97	89/93	100/90
N/S	16/-	12/4	12/3	12/4
TA/TD [s]	3.2/-	20.0/3.5(3.1)†	19.5/4.5	20.0/3
AF	2	12	11	16

Table 1. Acquisition parameters for different protocols. Their usage can be identified via the figure numbers. *Sampling* denotes the sampling percentage of the phase/slice encoding. Acquisition time (TA). * interpolated to 1.0 mm^2. † was used only once for phantom data in Figure 5

extracted flip angle map is spatially smoothed. We chose a signal-weighted linear filter of length 6, whose weights are determined by the average magnitude signal of the TI series. Subsequently, a two-parameter fit is performed with the FA map as prior information. Similarly to [34], fitting was implemented as a variable projection algorithm which reduces the non-linear least squares problem to a one-dimensional line search.

Data and acquisition setup

The proposed 3-D and reference 2-D LL imaging was performed in 11 healthy volunteers (5 female and 6 male, age 53±21 years) and in the ISMRM/NIST phantom [35]. The datasets were acquired on 1.5 T (n=5) and 3 T (n=6) clinical MR scanners (MAGNETOM Aera/Skyra, Siemens Healthcare, Erlangen, Germany) using prototypical Look-Locker sequences for the reference 2-D and the proposed 3-D acquisition. All protocol parameters are listed in Table 1 along with their figure location. Further, parallel imaging with acceleration factor (AF) of 2 was used for 2-D LL. The Poisson sampling parameters were ν = 2, R = 47 and θ = 0.75. For the non-selective inversion, an adiabatic tan/tanh pulse with 10 ms duration was utilized [36]. A fully sampled central k-space area of size 24×24 for sensitivity calibration is included in the scan time. Signal reception was performed with the table-mounted coil array and a flexible body coil array using a subset of 26-30 channels, depending on the field of view (FOV).

All reconstructions were performed using a prototype software on a clinical scanner hardware system (Octa-core, 2.1 GHz Intel Xeon processor). If not stated otherwise, 35 FISTA iterations with

regularization weights $\lambda_\sigma = 0.0006$ and $\lambda_\tau = 15\lambda_\sigma$ were used for 1.5 T and $\lambda_\sigma = 0.0003$ and $\lambda_\tau = 8\lambda_\sigma$ for 3 T.

Experiments and quality assessment

We performed a variety of experiments to evaluate the proposed 3-D LL method including its robustness on both phantom and volunteer data as well as the effect of regularization and sampling strategies. To test the accuracy and precision, the T_1 array of the ISMRM/NIST phantom was utilized. Nine spheres, which were filled with different concentrations of $NiCl_2$ to yield T_1 values in the range of 120 to 2000 ms were sampled. Ground-truth T_1 values for comparison were taken from IR measurements by Keenan et al. [35].

Initially, the impact of different reordering and segmentation schemes on the dynamic range of the relaxation as well as on T_1 accuracy was evaluated. To this end, the NIST phantom was acquired at 3 T using the same sampling pattern for each of the described segmentation/reordering schemes and reconstructed with identical parameters. Reference values of the phantom's T_1 array were used to calibrate the initial TI times for the three sampling schemes. Tube number six of the phantom with a T_1 at the lower end (350 ms) of the hepatic range was then selected for evaluating the signal relaxation curves. For all 9 spheres, the relative accuracy and precision was determined after calibrating the initial TI times for each sampling scheme to yield a high overall accuracy. Based on this criterion, one scheme was selected for all further experiments.

Before assessing the actual accuracy on phantom data, theoretically obtainable relaxation recovery and T_1 error rates (following the first inversion and delay time) for the protocols of this and a related study [20] were simulated as a function of T_1. Being the main focus, the range of abdominal T_1 values (300–1300 ms) was highlighted [2, 20]. Next, T_1 maps of the phantom were acquired and compared for a reference 2-D LL implementation and the proposed 3-D method (wedge sampling scheme) based on linear regression with known reference values. The mean absolute percentage error (MAPE) and the average ROI standard deviation (SD) were calculated. With the 3-D method, data was acquired at both 1.5 and 3 T.

Appropriate regularization weights are crucial for in-vivo imaging in the context of iterative reconstruction techniques. Their choice was based on qualitative and quantitative experiments for spatial and temporal regularization, respectively. An expert regularization was considered particurarly helpful for selecting spatial weights because they can have drastic impact on image impression while less affecting T_1. In order to find the option with the highest image quality w.r.t. both T_1 map and TI images, reconstructions from two exemplary datasets, one for each field strength with varying spatial ($\lambda_\sigma = 0.005/2^i, i \in [0;7]$) and temporal regularization ($\lambda_\tau = 64\lambda_\sigma/2^j, j \in [0;7]$) were shown to five oncology MRI experts with in average 16$\pm$11 years of experience. Their preferences were

consolidated by selecting the median vote for the decision of the spatial regularization parameter. The temporal regularization was selected according to an analysis of the relaxation curve and T_1 robustness for increasing temporal regularization using representative ROIs of liver and muscle tissue. The final selection criterion was the factor resulting in the minimum SD of the hepatic tissue.

Additionally to a qualitative comparison of representative T_1 maps as obtained with the 3-D and the 2-D method, the volunteer study included a T_1 evaluation of different abdominal tissue types in 11 volunteers grouped by acquisition method and field strength. To this end, several ROIs were drawn in slices from the 2-D reference acquisitions and matched with those in 3-D. Vessel structures in the liver were carefully spared. With a particular focus on the hepatic T_1, a further analysis of accuracy, variability and agreement between the proposed and the reference method was carried out.

RESULTS

Sampling strategy

The ability of different sampling strategies to capture the dynamics of the relaxation and to map T_1 values with a certain accuracy and precision is summarized in Figure 4. Aligning the sampled data points of the linear, the onion and the wedge scheme, it is possible to compare their dynamic ranges. Despite having yield very similar T_1 values (353-356 ms), the linear and the onion sampling captured only 44 % and 70 % of the initial dynamic as compared to the proposed wedge scheme. Evaluating T_1 accuracy on a larger range, the relative accuracy and precision as a function of T_1 varied broadly for the linear and the onion scheme, exceeding 10 % for low T_1 values. In average, the MAPE of the linear, onion and wedge scheme were 5.7 %, –5.1 % and 2.3 % with average SDs of 11.7 ms, 15.9 ms and 12.1 ms. Figure 4 also shows qualitative examples of a phantom acquisition using said sampling schemes.

Phantom study

Figure 5(a) shows signal recovery and T_1 error rates for various protocols. Our 3 T protocol attains above 95 % recovery until above 1900 ms while the ones for 1.5 T receive as much recovery until T_1 values of about 1320 ms and 1460 ms for a TD of 3.1 s and 3.5 s. With that, all protocols are below 5 % T_1 error for abdominal tissue. Dashed lines denote corresponding protocols of a related study for comparison. Figure 5(b-d) summarize the results of the linear regression and variability analysis between T_1 values obtained by phantom acquisitions and known ground-truth values. With a MAPE of 1.6 %, slope and bias of 1.0 and –5.8 ms, the proposed 3-D method achieved a slightly higher accuracy than the 2-D reference with 3.5 % MAPE and slope and bias of 1.1 and –16.7 ms at 3 T. At 1.5 T, results for the modified protocol with a shorter TD of 3.1 s were a slope and bias of 0.9

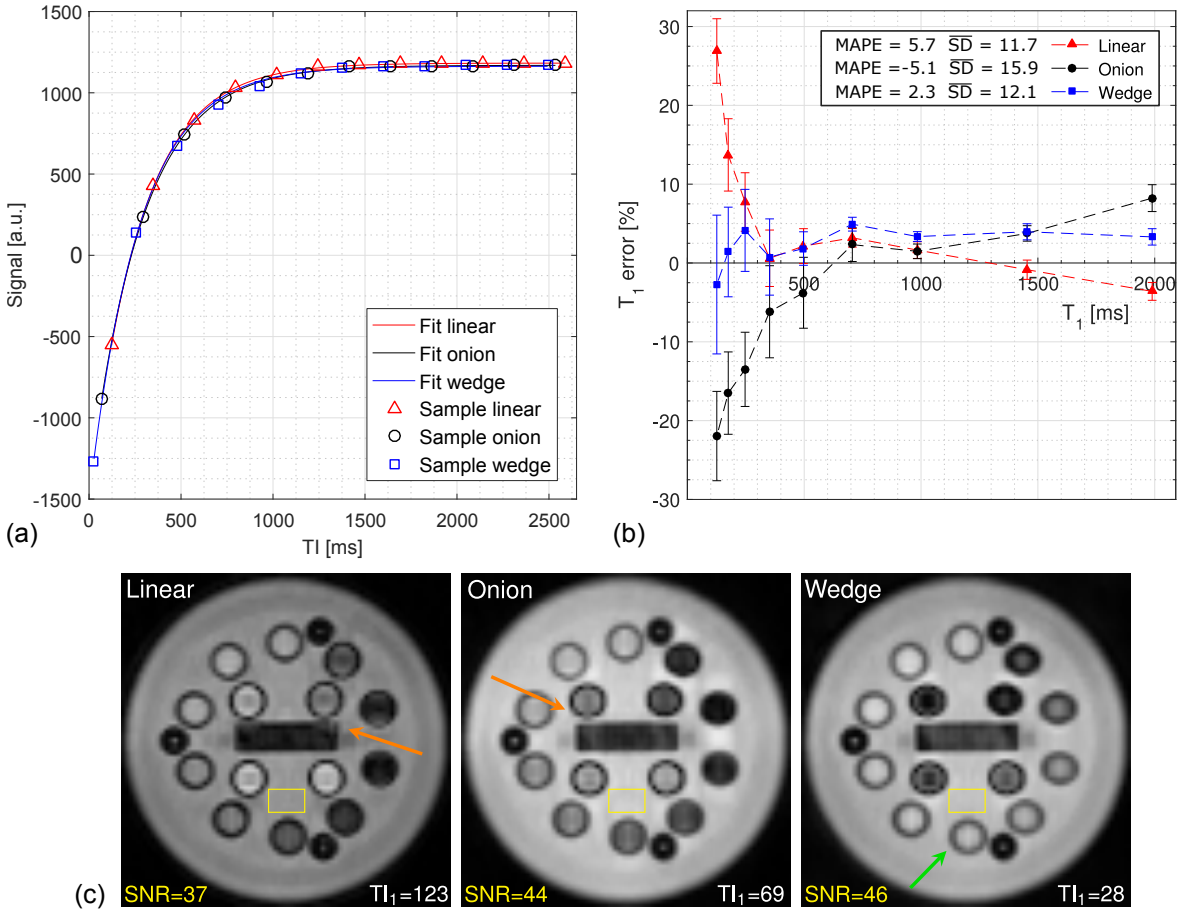

FIG. 4 Signal evolution of the 350 ms sample (green arrow) of the NIST phantom is shown for different segmentation and reordering schemes (a). Using appropriate initial TI values, the relaxation curves can be aligned, showing the differences in the captured dynamic range. Relative T_1 errors and SDs of the different sampling schemes are plotted as a function of T_1 (b). The average error and SD are reported too. A qualitative comparison of the approaches is shown for the first TI along with an SNR evaluation (yellow boxes) (c). Orange arrows indicate intensity artifacts

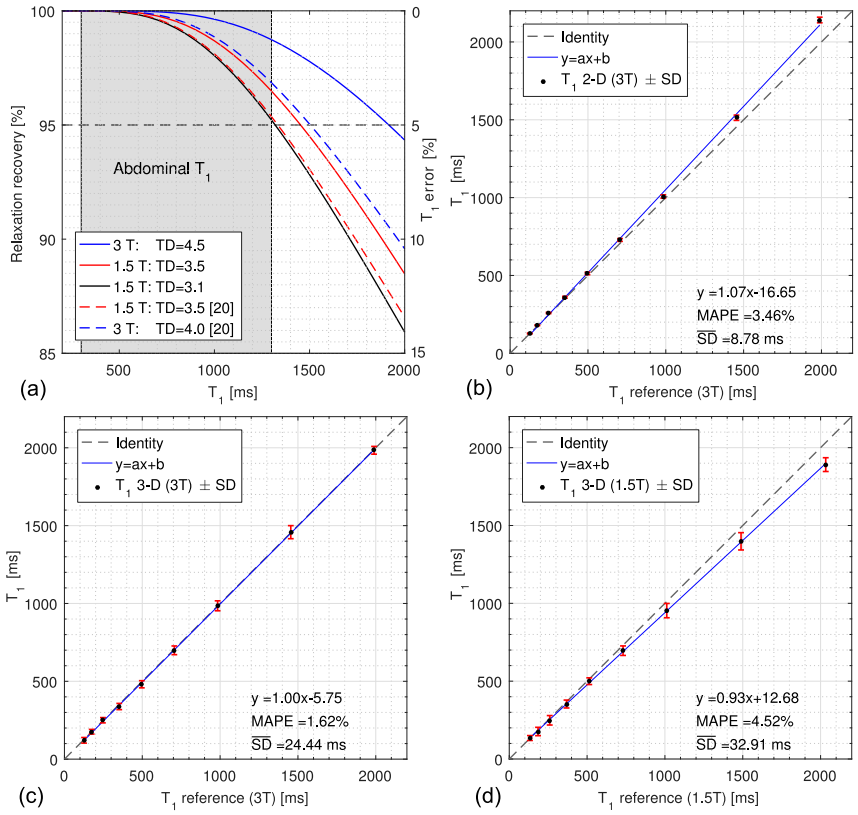

FIG. 5 Simulated relaxation recovery and T_1 error rates for various protocols (a). Comparison of T_1 accuracy and precision in the range of 0.1 to 2.0 s for acquisitions of the NIST phantom using a reference 2-D LL (only at 3 T) and the proposed 3-D sequence (c,d). Reference values are plotted against the measured ones along with their standard deviation (red). Identity is indicated by the dashed line whereas the blue line is the result of linear regression whose parameters are listed below along with the MAPE and the mean SD

and 12.7 ms and a MAPE of 4.5 %. The standard deviation (SD) increased for tubes with higher T_1 values and was in average 24.4 ms and 8.8 ms for 3-D and 2-D at 3 T, and 32.9 ms for 3-D at 1.5 T.

Evaluation of iterative reconstruction parameters

Figure 6 illustrates the qualitative evaluation of TI images and T_1 maps for one exemplary volunteer at 1.5 T by showing a subset of the options for spatio-temporal regularization that MR experts had to choose from. Preferred options are highlighted. As provided in Table 2, the preferences range more widely for the spatial weight at 1.5 T but yield higher consensus for the temporal regularization and at 3 T in general. The impact of varying regularization factors on the robustness of the relaxation curve and T_1 values in liver and muscle tissue is demonstrated in Figure 7. For increasing spatial regularization, the T_1 SD decreases while the T_1 itself tends to increase. The range of variation and the SD are larger for liver tissue likely due to its lower SNR. Temporal regularization with very high factors caused a signal underestimation of the initial relaxation whereas very low factors lead to high

Category	Expert 1	Expert 2	Expert 3	Expert 4	Expert 5	**Median**
1.5 T spatial (i)	3	4	2	5	1	3
1.5 T temporal (j)	1	1	3	1	1	1
3 T Spatial (i)	4	4	5	5	4	4
3 T Temporal (j)	3	2	3	4	2	3

Table 2. Image preferences of five MR experts for spatial and temporal regularization factors using volunteer datasets at both field-strengths. The median vote marks the final choice. The selection options from 0 to 7 correspond to the regularization weights as described on page 11

variability in between TIs towards the steady-state. For the large range of temporal regularization weights, T_1 varies within a range of 5 % and 2 % for liver and muscle tissue. This difference seems to be in accordance with their SNR values of about 17 and 28. Finally, the SD as a function of temporal regularization forms a minimum at about the same range of weights for both tissue types.

In-vivo study

Qualitative results of three exemplary volunteers are presented for comparison in Figure 8 for the proposed 3-D and reference 2-D method. In addition to the axial views, coronal or sagittal reformatting was possible for the 3-D data. For some volunteers, 3-D scans with a higher resolution, being closer to that of the reference, were additionally acquired in about the same time by using higher undersampling and shorter delays (*cf.* Table 1). The overall reconstruction time of the 3-D TI data with the above protocol parameters was less than 3 min and about 30 s for T_1 mapping.

Average T_1 values along with their ROI SD and inter-subject variability (variation of mean T_1 values among subjects) as obtained from 11 volunteers by the proposed and the reference method can be found in Table 3. While the T_1 SD is similar at the higher field strength, it is 40 %, 45 % and 28 % lower in liver, spleen and muscle tissue for 3-D at 1.5 T. Focusing on liver tissue in more detail, the agreement between T_1 values obtained by the two methods as well as its precision is summarized in the scatter and Bland-Altman plots of Figure 9. The average differences between the methods were -10 and 1 ms for 1.5 and 3 T but the confidence interval for the lower field-strength was half as wide compared to 3 T.

DISCUSSION

We developed a 3-D Cartesian Look-Locker technique that is able to perform whole liver T_1 mapping within a single breath-hold using sparse sampling and spatio-temporally constrained reconstruction. An essential feature is the k-space segmentation as it allows for a 3- to 4-fold increase in temporal

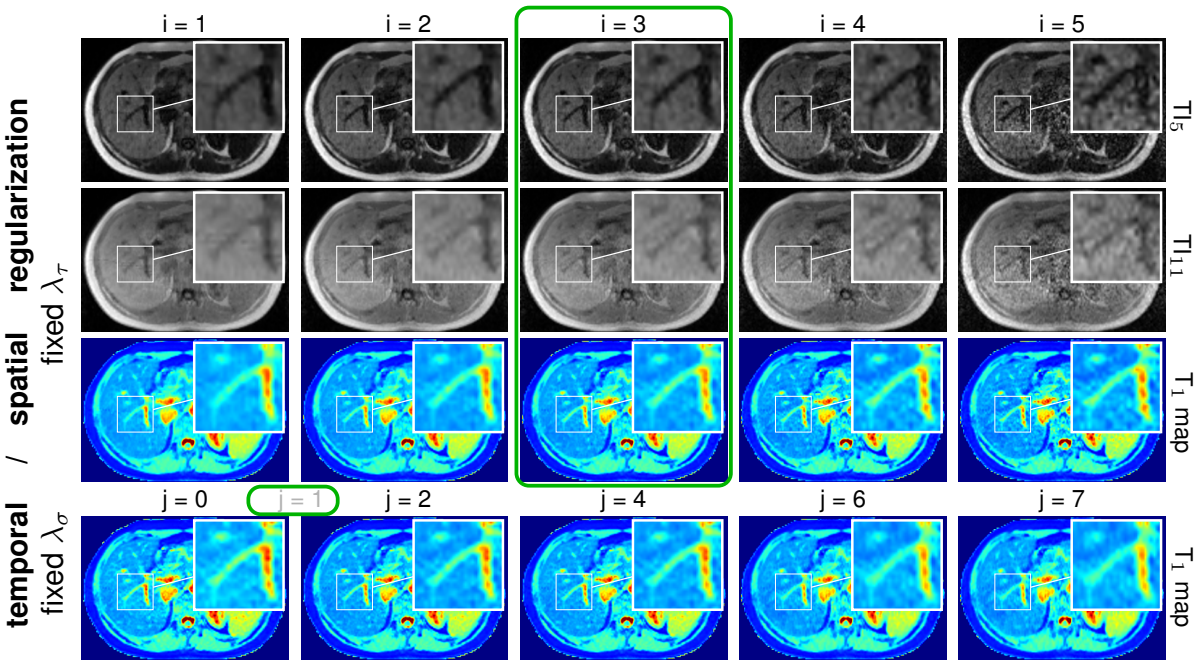

FIG. 6 An exemplary volunteer dataset was reconstructed with varying spatial and temporal regularization weights to find the optimal reconstruction parameters by visual inspection. Two contrast images (after zero crossing and towards steady state) and the corresponding T_1 map at 1.5 and 3 T were rated by five MR experts. A subset of the images for 1.5 T is shown, where the effects of increasing spatial (temporal) regularization weights for a fixed temporal (spatial) factor are observable. Preferred choices are outlined in green (*cf.* Table 2)

resolution, which is required to robustly determine T_1 in the case of rapid relaxation. In this context, we showed that the actual segmentation and reordering scheme vastly impacts the ability to capture the full dynamics of the relaxation and thereby T_1 accuracy. The reduced signal amplitude using a linear or onion scheme, up to 44 % compared to the wedge scheme, caused considerable inaccuracies for T_1 values below 300 ms. Further, we observed different degrees of blur or intensity artifacts on phantom (*cf.* Figure 4) and in-vivo data depending on the actual segmentation and reordering. Other studies reported similar findings, particularly for the linear case [26]. These effects could be due to variation among the density within segments affecting the effective time at which k-space center points are sampled, which depends on asymmetry from variable density and non-quadratic FOVs too.

A validation of the proposed method based on the NIST phantom revealed excellent agreement with known reference values. At 3 T, very high accuracy was achieved in the whole T_1 range while the 2-D reference tended to overestimate higher values (Figure 5). For 1.5 T, excellent accuracy was achieved from 120 to 1000 ms. Declining accuracy towards very high T_1 values, above 1500 ms, can be attributed to a shortened TD of 3.1 s as compared to 3.5 s used in-vivo and 4.5 s as used for 3 T.

	1.5 T		3 T	
Tissue	3-D	2-D	3-D	2-D
Liver	$554 \pm 37\,(33)$	$544 \pm 52\,(25)$	$767 \pm 44\,(111)$	$768 \pm 44\,(117)$
Spleen*	$1064 \pm 69\,(47)$	$1106 \pm 100\,(43)$	$1381 \pm 64\,(80)$	$1403 \pm 75\,(64)$
Muscle*	$892 \pm 36\,(17)$	$876 \pm 46\,(16)$	$1206 \pm 54\,(68)$	$1173 \pm 52\,(45)$

Table 3. Average T_1 values [ms] along with their ROI standard deviation and inter-subject variability (bracketed) for the evaluated tissues in 11 volunteers. *Total number of cases reduced to 8 since the organ was not acquired in 2-D

This is supported by the simulations on signal recovery and T_1 error rates, which show the trends between the setups clearly. But focusing on abdominal T_1 only, all protocols yield theoretical T_1 errors below 5 %. The measured T_1 variability in the phantom was more than twice as high for 3-D compared to 2-D at 3 T and further increased at the lower field-strength. As this relation was not seen in-vivo, it can likely be attributed to the small sample size of the phantom spheres comprising only about 10 pixels for the 3-D protocol but 8-fold as many for 2-D. These differences can be seen in similar studies involving 3-D/2-D phantom/in-vivo data too, e.g. [11].

The choice of regularization parameters for the iterative reconstruction is crucial as it controls the balance between a potential loss of features through over-regularization and aliased images with grainy noise in the case of under-regularization. Although quantitative techniques exist to determine the optimal choice for specific criteria such as the L-curve [37], it remains a topic of ongoing research in general. However, we addressed this issue by considering both visual ratings from five MR experts and technical criteria related to T_1 variability. The T_1 SD as a function of temporal weight suggested a range with lowest SD quite clearly (see Figure 7). The rationale behind this region with minimal SD is that a too low regularization weight preserves most variations such as noise and artifacts in the temporal domain, while very high factors tend to shortcut the relaxation, thereby again increasing the differences between neighboring contrasts. Using this criterion, the final choice was more conservative than the experts' consensus, which rated for a slightly higher temporal regularization. The T_1 values themselves seemed to be quite robust against increasing regularization: even for rather extreme regularization weights, the variation did not exceed a range of 5 % and 2 % for liver and muscle tissue, which is less than their SD. The higher variation for liver tissue is what we attribute to its lower SNR since the evaluated muscle tissue (back) is closer to the receiving coil elements. A similar effect was observed when considering effects of spatial regularization. However, here the SD consistently decreased with stronger regularization whereas the T_1 itself tended

to increase. This is explicable by considering that too strong regularization thresholds actual signal instead of noise, which largely affects small intensities causing steeper relaxing curves. Considering that for varying spatial regularization, small changes in T_1 can translate to considerable changes in image appearance (*cf.* Figure 6), we favored the experts' decision over quantitative measures.

The comparison of T_1 values in 11 volunteers showed very high agreement between the proposed and the reference method at both field-strengths. Also, the confidence intervals of the differences between hepatic T_1 values are as low or lower than the measured tissue variability (see Table 3 and Figure 9). In striking contrast to the findings from phantom data, the T_1 variability in 3-D and 2-D data is similar for the higher field but up to 45 % lower for 3-D at 1.5 T. A hepatic T_1 SD of 6.7 % and 5.7 % of its mean for 1.5 and 3 T compares favorably with current work, particularly in view of the high undersampling factor [20]. A low apparent signal-to-noise ratio (SNR) in the FOV center is symptomatic for high resolution abdominal 2-D imaging, and the observation that the SNR differences vanish at 3 T suggests that the SNR gain at 1.5 T can be attributed to the acquisition in 3-D (despite a low flip angle setup) and the intrinsic spatio-temporal denoising during the iterative reconstruction.

The qualitative comparison in three volunteers shows T_1 maps with a well comparable impression between 3-D and 2-D acquisitions (see Figure 8). The axial views in 2-D are of higher resolution, offering a little more detail on vessels and sharp edges, albeit with considerable fine grained noise particularly for the lower field strength. The presented 3-D scan with a similarly high spatial resolution achieved a comparable image impression and noise characteristic. In general, a major benefit of the 3-D acquisition is the volumetric coverage that offers among other benefits coronal or sagittal views as well as volumetric organ analysis.

Another key feature of the proposed approach is the variable density sampling with high sparsity and additional temporal incoherence. Our novel extension for spatio-temporally incoherent Poisson sampling was developed for multi-contrast or dynamic imaging to provide improved k-space coverage and incoherence over conventional Poisson disc sampling (see Figure 2). Above that, with 0.3 s for generating and segmenting patterns of a typical protocol, the sampling can be implemented fast enough to be used online.

Generally, one major drawback of segmentation with a signal model that requires full relaxation is the poor scan efficiency. In fact, our protocols use only about half of the breath-hold time for signal reception. With higher fields and increasing T_1 values, the time for full relaxation increases as well. Yet, at the same time it is sufficient to use a lower temporal resolution and with that either less segmentation or acceleration. With the above protocol, we can accurately determine T_1 values down to 120 ms for which there is currently no clinical application with the exception of, e.g., cardiac function analysis [38]. Consequently, a shorter scan time, higher resolution imaging or sharper

images due to less sparse sampling are readily available by reducing the number of segments, i.e. the temporal resolution. We chose wait times consistent with or more conservatively than in previous studies [20], because we too observed how residual magnetization differences between k-space segments can degrade image quality [26]. But even with the same delay times, our protocols can attain more recovery compared to [20], primarily due to utilizing smaller FAs (*cf.* Figure 5). Notice that a zero wait time sacrifices B_1 robustness, which is crucial for abdominal imaging and enables the Look-Locker technique to be superior to VFA methods. Alternatively following [12, 39], one could introduce an initial magnetization preparation to cut wait times down to the order of T_1 values for the cost of a reduced dynamic range, i.e. fit precision.

A further remark, the inversion quality was not modeled or corrected as this seemed a negligible source of error given the utilized adiabatic inversion. However, by switching from a longer bell-shaped hyperbolic secant to a shorter square tan/tanh pulse, we noticed a slight improvement in the dynamic range as well as in the SD [36].

Although reconstruction times of less than four minutes are generally competitive, they may not be tolerable in every clinical setting. Hence, an approximately 5-fold further reduction in processing time without yet considering coil compression can be gained from a (multi-)GPU implementation [21]. Finally, a comparison to previous compressed sensing methods is difficult since they are mostly based on either VFA methods with retrospective undersampling [16, 18], or based on 2-D LL techniques using radial readouts [19] or retrospective experiments [17]. Commonly, 3-D VFA has been compared using the ratio of *number of measurements*/*acceleration factor*. These works, which were validated using retrospective undersampling only, achieve a ratio of 1.6 as compared to 1.0 of our proposed method. At the same time, the reported reconstruction times can lie in order of hours [18]. In future work, we plan to validate the feasibility of the proposed method in patients too.

CONCLUSION

We developed a 3-D Cartesian Look-Locker technique that is able to map T_1 in the whole liver within a single breath-hold. Through the combination of a segmentation strategy that is dedicated to the LL scheme and a novel spatio-temporally incoherence for Poisson sampling, the accuracy of conventional 2-D LL can be achieved, but with the large volumetric coverage that is usually only feasible with VFA methods. A thorough validation on phantom as well as volunteer data showed excellent agreement with known values and the reference method. Typical challenges in a clinical setting such as sampling bias, multiple scans to include large or missed organs could be tackled via such a fast and accurate volumetric T_1 mapping technique.

ACKNOWLEDGEMENTS

This work was partly supported by the Research Training Group 1773 “Heterogeneous Image Systems”, funded by the German Research Foundation (DFG).

COMPLIANCE WITH ETHICAL STANDARDS

Informed consent This manuscript does not contain clinical studies or patient data. Informed consent was obtained from all volunteers included in the study.

Conflict of interest Felix Lugauer, Jens Wetzl and Manuel Schneider receive project funding from Siemens Healthcare GmbH. Christoph Forman, Dominik Nickel and Berthold Kiefer are employees of Siemens Healthcare GmbH.

Authors' contribution Lugauer: Protocol and project development, data collection and analysis. Forman: Protocol and project development, data analysis. Wetzl: Protocol and project development, data collection. Schneider: Data collection and management. Kiefer: Project development. Hornegger: Project development. Nickel: Protocol and project development, data analysis. Maier: Project development.

APPENDIX

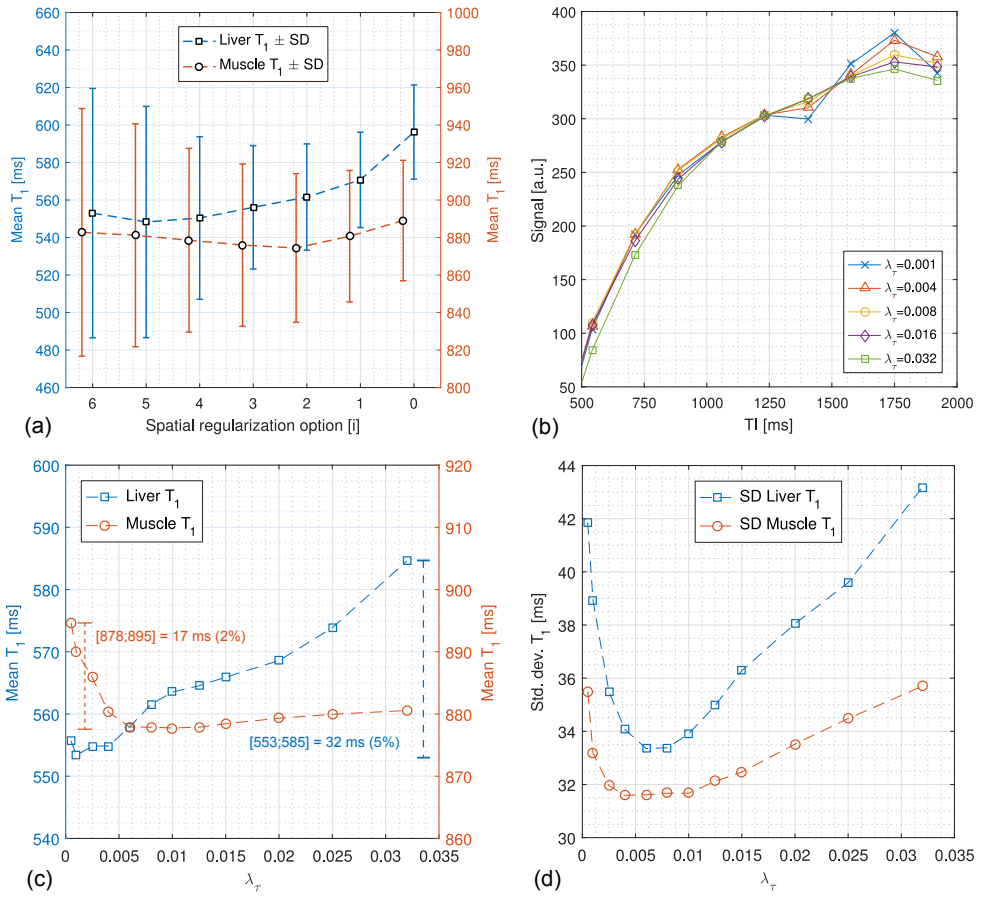

FIG. 7 The effect of varying regularization factors for an exemplary liver and muscle ROI at 1.5 T: T_1 mean and SD for different spatial regularization options (a). For better visibility, a linear range of regularization options was used (i.e. decreasing regularization strength from left to right), including a small offset to distinguish liver and muscle tissue. Effect of temporal regularization on the hepatic relaxation curve (b): for small regularization factors, there is a high variability between TIs towards the steady state, while very high factors tend to underestimate the high dynamics at the beginning relaxation. T_1 mean (c) and SD (d) for increasing temporal regularization. The range of T_1 variation is 5 % and 2 % for liver and muscle. The SDs of both tissue types show minimal values at about the same regularization factor

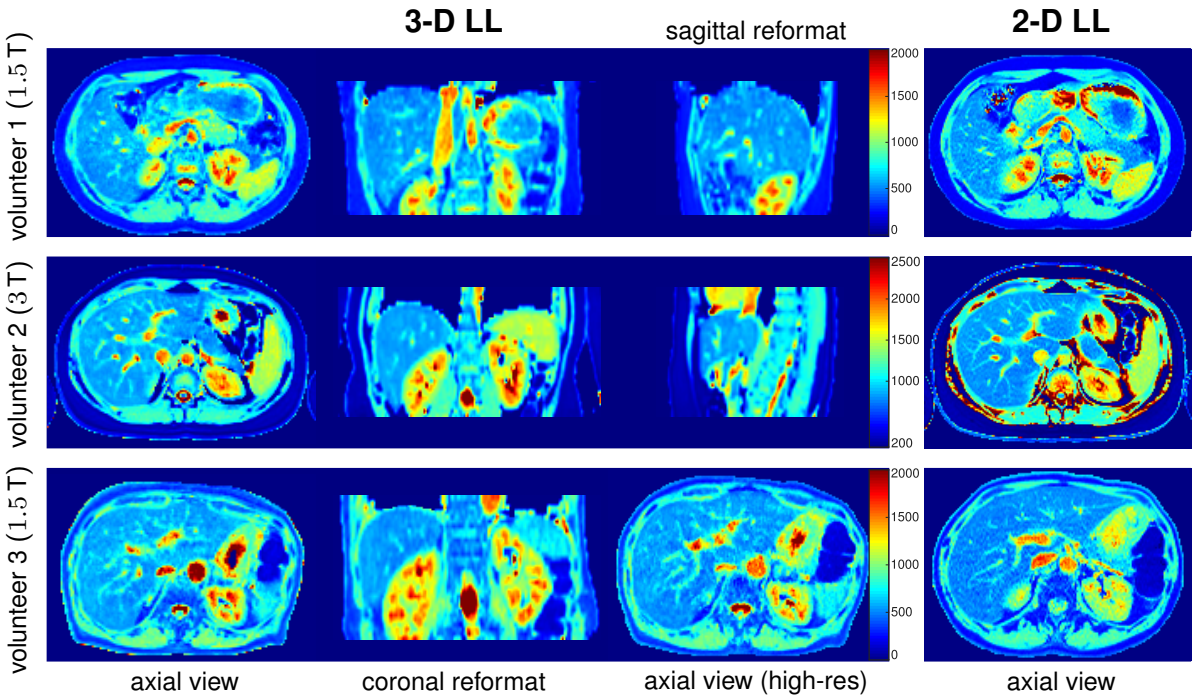

FIG. 8 Qualitative comparison of T_1 maps as obtained by 3-D and reference 2-D LL for three exemplary datasets. T_1 maps of the reference were restricted to few axial views (interpolated 1 mm^2 with 8 mm slice thickness) per breath-hold while the 3-D acquisition with 30 slices enabled the usage of reformatted views. For some volunteers (here, #3) higher resolution protocols were acquired as well (*cf.* Table 1). The intensity scale applies for both 2-D and 3-D

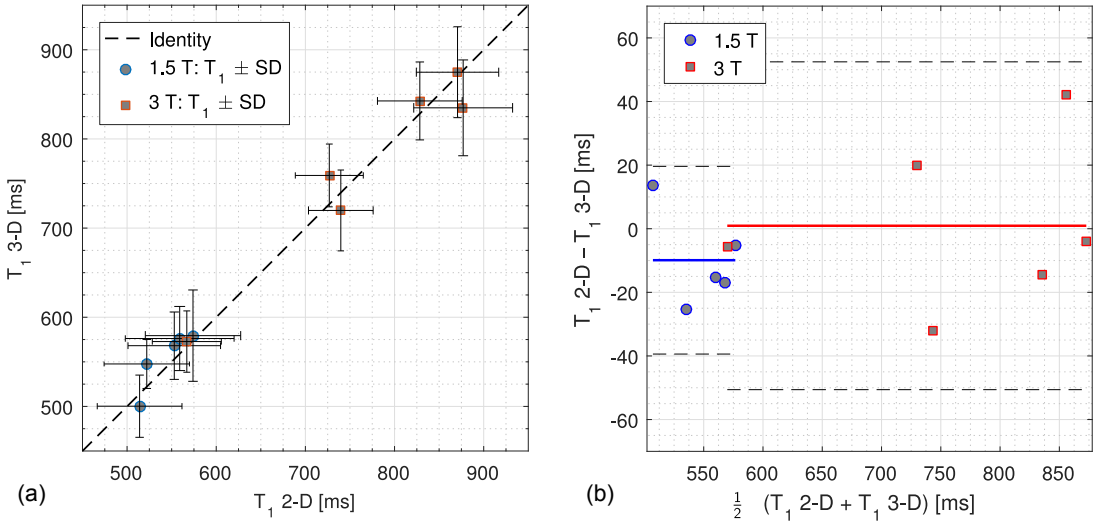

FIG. 9 Quantitative comparison of the average hepatic T_1 as obtained by the proposed 3-D and reference 2-D method in 11 volunteers: a scatter plot shows the agreement between T_1 values along with its SD (a). The average differences between the methods are indicated by a blue and red line for 1.5 and 3 T (-10 and 1 ms), along with its confidence intervals (dotted lines) in the Bland-Altman plot (b)

Algorithm 1: 2-D+t Poisson sampling with variable density and incoherence

Input: $N_y, N_z, R, n, \theta, m_a, r_{min} \leftarrow 0.634, \rho \leftarrow$(Eqs. (1) and (3))

Output: Mask $\boldsymbol{M}$ of size $N_y \times N_z$

`seed`(n) `// Deterministic but different masks for each` n

$l_{active} \leftarrow ()$

$\boldsymbol{p} \leftarrow (N_y/2, N_z/2)$ `// Start at the center or add a jitter`

$l_{active} \leftarrow (l_{active}, \boldsymbol{p})$ `// Add to the list of active points`

$\boldsymbol{M}(\boldsymbol{p}) \leftarrow 1, \boldsymbol{M}_a(\boldsymbol{p}) \leftarrow \boldsymbol{M}_a(\boldsymbol{p}) + 1$ `// Set and accumulate masks`

while $l_{active} \neq ()$ **do**

  $\boldsymbol{p}_c \leftarrow$ `pop`(l_{active}) `// Take out first or any existing point`

  $\rho_c \leftarrow \rho(\boldsymbol{p}_c)$

  `// Generate up to` R `points from current position and density`

  for $i \leftarrow 1$ **to** R **do**

    `// Random uniform numbers in the range [a,b)`

    $r_c \leftarrow$ `randu`$(r_{min}/\rho_c, 2r_{min}/\rho_c)$, $\alpha_c \leftarrow$ `randu`$(0, 2\pi)$

    $\boldsymbol{p} \leftarrow \boldsymbol{p}_c + (\lceil$`cos`$(\alpha_c) r_c \rceil, \lceil$`sin`$(\alpha_c) r_c \rceil)$

    if $\boldsymbol{p} \neq \boldsymbol{p}_c$ ***and*** `insideBounds`$(\boldsymbol{p}, N_y, N_z)$ **then**

      `// Sampled too often according to Eq. (4)`

      if `lacksIncoherence`$(\boldsymbol{p}, \boldsymbol{M}_a, t, \theta)$ **then** continue

      `// Distance to nearby existing points smaller` $r_{min}/\rho(\boldsymbol{p}))$

      if `anyPointWithinRadius`$(\boldsymbol{p}, \boldsymbol{M}, r_{min}/\rho(\boldsymbol{p}))$ **then** continue

      $l_{active} \leftarrow (l_{active}, \boldsymbol{p})$

      $\boldsymbol{M}(\boldsymbol{p}) \leftarrow 1, \boldsymbol{M}_a(\boldsymbol{p}) \leftarrow \boldsymbol{M}_a(\boldsymbol{p}) + 1$

REFERENCES

[1] Tirkes T, Lin C, Fogel EL, Sherman SS, Wang Q, Sandrasegaran K (2017) T1 mapping for diagnosis of mild chronic pancreatitis. J Magn Reson Imaging 45(4):1171–1176

[2] Haimerl M, Verloh N, Zeman F, Fellner C, Müller-Wille R, Schreyer AG, Stroszczynski C, Wiggermann P (2013) Assessment of clinical signs of liver cirrhosis using T1 mapping on Gd-EOB-DTPA-enhanced 3T MRI. PLoS One 8(12):e85658

[3] Yoon JH, Lee JM, Kim E, Okuaki T, Han JK (2017) Quantitative liver function analysis: volumetric T1 mapping with fast multisection B1 inhomogeneity correction in hepatocyte-specific contrast-enhanced liver MR imaging. Radiology 282(2):408–417

[4] Huang Y, Sadowski EA, Artz NS, Seo S, Djamali A, Grist TM, Fain SB (2011) Measurement and comparison of T1 relaxation times in native and transplanted kidney cortex and medulla. J Magn Reson Imaging 33(5):1241–1247

[5] Look DC, Locker DR (1970) Time saving in measurement of NMR and EPR relaxation times. Rev Sci Instrum 41(2):250–251

[6] Deichmann R, Haase A (1992) Quantification of T1 values by SNAPSHOT-FLASH NMR imaging. J Magn Reson 96(3):608–612

[7] Deoni SC, Rutt BK, Peters TM (2003) Rapid combined T1 and T2 mapping using gradient recalled acquisition in the steady state. Magn Reson Med 49(3):515–526

[8] Fellner C, Verloh N, Haimerl M, Kubach MR, Nickel MD, Schlabeck M, Stroszczynski C, Wiggermann P (2014) T1 mapping of the whole liver in a single breath hold at 3T. In: Proceedings of the 22nd scientific meeting, International Society for Magnetic Resonance in Medicine, Milano, p 3235

[9] Deoni SC (2007) High-resolution T1 mapping of the brain at 3T with driven equilibrium single pulse observation of T1 with high-speed incorporation of RF field inhomogeneities (DESPOT1-HIFI). J Magn Reson Imaging 26(4):1106–1111

[10] Henderson E, McKinnon G, Lee TY, Rutt BK (1999) A fast 3D Look-Locker method for volumetric T1 mapping. Magn Reson Imaging 17(8):1163–1171

[11] Kimelman T, Vu A, Storey P, McKenzie C, Burstein D, Prasad P (2006) Three-dimensional T1 mapping for dGEMRIC at 3.0 T using the Look Locker method. Invest Radiol 41(2):198–203

[12] Shah N, Zaitsev M, Steinhoff S, Zilles K (2001) A new method for fast multislice T1 mapping. Neuroimage 14(5):1175–1185

[13] Eldeniz C, Finsterbusch J, Lin W, An H (2016) TOWERS: T-One with Enhanced Robustness and Speed. Magn Reson Med 76(1):118–126

[14] Lustig M, Donoho D, Pauly JM (2007) Sparse MRI: The application of compressed sensing for rapid MR imaging. Magn Reson Med 58(6):1182–1195

[15] Jung H, Sung K, Nayak KS, Kim EY, Ye JC (2009) k-t FOCUSS: A general compressed sensing framework for high resolution dynamic MRI. Magn Reson Med 61(1):103–116

[16] Velikina JV, Alexander AL, Samsonov A (2013) Accelerating MR parameter mapping using sparsity-promoting regularization in parametric dimension. Magn Reson Med 70(5):1263–1273

[17] Doneva M, Börnert P, Eggers H, Stehning C, Sénégas J, Mertins A (2010) Compressed sensing reconstruction for magnetic resonance parameter mapping. Magnetic Resonance in Medicine 64(4):1114–1120

[18] Zhang T, Pauly JM, Levesque IR (2015) Accelerating parameter mapping with a locally low rank constraint. Magn Reson Med 73(2):655–661

[19] Tran-Gia J, Bisdas S, Köstler H, Klose U (2016) A model-based reconstruction technique for fast dynamic T1 mapping. Magn Reson Imaging 34(3):298–307

[20] Chen Y, Lee GR, Aandal G, Badve C, Wright KL, Griswold MA, Seiberlich N, Gulani V (2016) Rapid volumetric T1 mapping of the abdomen using three-dimensional through-time spiral GRAPPA. Magn Reson Med 75(4):1457–1465

[21] Wetzl J, Schmidt M, Pontana F, Longère B, Lugauer F, Maier A, Hornegger J, Forman C (2017) Single-breath-hold 3-D CINE imaging of the left ventricle using Cartesian sampling. Magn Reson Mater Phy. doi:10.1007/s10334-017-0624-1

[22] Lugauer F, Wetzl J, Forman C, Schneider M, Kiefer B, Nickel D, Maier A (2017) Single breath-hold abdominal T1 mapping using 3-D Cartesian sampling and spatiotemporally constrained reconstruction. In: Proceedings of the 25th scientific meeting, International Society for Magnetic Resonance in Medicine, Honolulu, p 68

[23] Bridson R (2007) Fast Poisson disk sampling in arbitrary dimensions. In: ACM SIGGRAPH 2007 Sketches. doi:10.1145/1278780.1278807

[24] Lugauer F, Nickel D, Wetzl J, Kiefer B, Hornegger J, Maier A (2017) Accelerating multi-echo water-fat MRI with a joint locally low-rank and spatial sparsity-promoting reconstruction. Magn Reson Mater Phy 30:189–202

[25] Levine E, Daniel B, Vasanawala S, Hargreaves B, Saranathan M (2017) 3D Cartesian MRI with compressed sensing and variable view sharing using complementary poisson-disc sampling. Magn Reson Med 77(5):1774–1785

[26] Hui C, Esparza-Coss E, Narayana PA (2013) Improved three-dimensional Look–Locker acquisition scheme and angle map filtering procedure for T1 estimation. NMR Biomed 26(11):1420–1430

[27] Wilman AH, Riederer SJ (1997) Performance of an elliptical centric view order for signal enhancement and motion artifact suppression in breath-hold three-dimensional gradient echo imaging. Magn Reson Med 38(5):793–802

[28] Saranathan M, Tourdias T, Bayram E, Ghanouni P, Rutt BK (2015) Optimization of white-matter-nulled magnetization prepared rapid gradient echo (MP-RAGE) imaging. Magnetic Resonance in Medicine 73(5):1786–1794

[29] Pruessmann KP, Weiger M, Scheidegger MB, Boesiger P et al (1999) SENSE: sensitivity encoding for fast MRI. Magn Reson Med 42(5):952–962

[30] Beck A, Teboulle M (2009) A fast iterative shrinkage-thresholding algorithm for linear inverse problems. SIAM J Imaging Sci 2(1):183–202

[31] Liu J, Rapin J, Chang Tc, Lefebvre A, Zenge M, Mueller E, Nadar MS (2012) Dynamic cardiac MRI reconstruction with weighted redundant Haar wavelets. In: Proceedings of the 20th scientific meeting, International Society for Magnetic Resonance in Medicine, Melbourne, p 178

[32] Guerquin-Kern M, Häberlin M, Pruessmann KP, Unser M (2011) A fast wavelet-based reconstruction method for magnetic resonance imaging. IEEE Trans Med Imaging 30(9):1649–1660

[33] Deichmann R (2005) Fast high-resolution T1 mapping of the human brain. Magn Reson Med 54(1):20–27

[34] Barral JK, Gudmundson E, Stikov N, Etezadi-Amoli M, Stoica P, Nishimura DG (2010) A robust methodology for in vivo T1 mapping. Magn Reson Med 64(4):1057–1067

[35] Keenan KE, Stupic KF, Boss MA, Russek SE, Chenevert TL, Prasad PV, Reddick WE, Zheng J, Hu P, Jackson EF (2016) Comparison of T1 measurement using ISMRM/NIST system phantom. In: Proceedings of the 24th scientific meeting, International Society for Magnetic Resonance in Medicine, Singapore, p 3290

[36] Kellman P, Herzka DA, Hansen MS (2014) Adiabatic inversion pulses for myocardial T1 mapping. Magn Reson Med 71(4):1428–1434

[37] Hansen PC (1992) Analysis of discrete ill-posed problems by means of the L-curve. SIAM Rev 34(4):561–580

[38] Wetzl J, Stalder AF, Schmidt M et al (2016) Joint estimation of cardiac motion and T1 maps for magnetic resonance late gadolinium enhancement imaging. In: Ourselin S, Joskowicz L, Sabuncu MR, Unal G, Wells W, eds., "Medical Image Computing and Computer-Assisted Intervention – MICCAI 2016: 19th International Conference, Athens, Greece, October 17-21, 2016, Proceedings, Part III, Springer, pp 527–535

[39] Deichmann R, Hahn D, Haase A (1999) Fast T1 mapping on a whole-body scanner. Magn Reson Med 42(1):206–209